

**Localized to itinerant transition of  $f$  electrons in ordered Ce films on W(110)**Q. Y. Chen, W. Feng,<sup>\*</sup> D. H. Xie, X. C. Lai, X. G. Zhu,<sup>†</sup> and L. Huang<sup>‡</sup>*Science and Technology on Surface Physics and Chemistry Laboratory, Mianyang 621908, China*

(Received 2 November 2017; revised manuscript received 18 March 2018; published 26 April 2018)

A key issue to understand the driving force and underlying physics in the isostructural  $\gamma$ - $\alpha$  transition in Cerium is the character of the  $4f$  states, whether it is localized or itinerant. Here the surface topography and electronic structure of the well-ordered Ce metal films on a W(110) substrate were investigated by using scanning tunneling microscopy, angle-resolved photoemission spectroscopy and density functional theory, and single-site dynamical mean-field theory calculations. Three nearly flat  $f$  bands can be observed, and a weakly dispersive quasiparticle band near the Fermi level has been directly observed at low temperature, indicating the hybridization between  $f$  electrons and conduction electrons in the low-temperature  $\alpha$  phase. The hybridization strength becomes weaker upon increasing temperature, and the  $f$  electrons become almost fully localized at 300 K in the high-temperature  $\gamma$  phase. The observed localized-to-itinerant transition of the  $f$  electrons with decreasing temperature gives direct experimental proof for the changes of the  $4f$  character in the isostructural  $\gamma$ - $\alpha$  phase transition. Our results suggest that the character of the  $f$  electrons plays a crucial role during the  $\gamma$ - $\alpha$  phase transition.

DOI: [10.1103/PhysRevB.97.155155](https://doi.org/10.1103/PhysRevB.97.155155)**I. INTRODUCTION**

Cerium, being one of the most mysterious and interesting elements in the periodic table, undergoes an isostructural  $\gamma$ - $\alpha$  phase transition (both phases are in face-centered-cubic structure), which is accompanied by a volume collapse of 15% at room temperature and ambient pressure [1]. The magnetic properties also exhibit a change from localized magnetic moments in the  $\gamma$  phase to Pauli paramagnetism in the  $\alpha$  phase [2,3]. Although the underlying physics and driving force of the  $\gamma$ - $\alpha$  phase transition have been studied extensively [4–9], it has been, and continues to be, warmly debated. Up to now, two prevalent scenarios are: the Mott transition for the  $f$  electrons and the Kondo volume collapse. In the Mott scenario [10], the hybridization between  $f$  orbitals is believed to change across the transition, leading delocalized  $f$  electrons in the  $\alpha$  phase, and localized  $f$  states in the  $\gamma$  phase. While in the Kondo volume collapse scenario [1,11], the transition was connected with modifications in the effective hybridization of the  $spd$  bands with the  $f$  electrons. The main change when going from  $\alpha$  to  $\gamma$  is the degree of hybridization and hence the Kondo scale. Despite numerous studies that seem to support one or the other model, it appears that a consensus on the nature of the phase transition has not yet been reached.

Although a conclusive answer regarding the driving force of this transition is still lacking, the role of the  $f$  electrons is expected to play a crucial role. The character of the  $f$  electrons, whether localized or itinerant, has been studied by many groups both experimentally and theoretically [4–9]. General agreement has been reached that the  $f$  electrons are predominantly localized in the high-temperature  $\gamma$  phase, while

conflicting results have been suggested for the low-temperature  $\alpha$  phase. Neutron inelastic scattering measurements provided evidence for the localized character of the  $4f$  states in the  $\alpha$  phase [12]. While optical conductivity measurements observed significant changes between  $\alpha$  and  $\gamma$ -Ce [13]. Meanwhile, x-ray absorption [14], x-ray photoemission spectroscopy [15,16], resonant photoemission studies [17], and inverse photoelectron spectroscopy [18,19] all suggested that the  $4f$ -state derived peak at the Fermi level ( $E_F$ ) is pronounced in the  $\alpha$  phase, which is originated from the itinerant  $f$  states.

A very powerful tool which allows direct observation of the behavior of the  $f$  electrons is angle-resolved photoemission spectroscopy (ARPES). The earliest ARPES measurements were performed on a well-ordered  $\gamma$ -Ce(001) single-crystal surface, and good agreement for the band structure is found between experimental and calculations [20]. The surface states of ordered  $\gamma$ -like Ce films on W(110) and the splitting of the  $4f^0$  ionization peak has been studied by Laubschat's group [21,22], and the Ce  $4f$  states are found to form a band and hybridization predominantly occurs between the  $4f$  and the valence state at the same wave vector. The evolution of  $\gamma$ - $\alpha$ - $\gamma$ -like phase transition of Ce was observed with increasing Ce coverage [23,24], and it is proposed that Ce ordered overlayers on various thickness grown on appropriate substrates may tune the hybridization strength. These results throw new light on the investigation of the  $\gamma$ - $\alpha$  transition. However, all these ARPES measurements have been performed at room temperature and mainly focused on the high-temperature  $\gamma$  phase, direct experimental proof for the localization-delocalization process during the  $\gamma$ - $\alpha$  phase transition as a function of temperature is still lacking.

Here well-ordered Ce epitaxial films were grown on a W(110) surface, and the surface topographies of the films have been studied by scanning tunneling spectroscopy (STM). Detailed electronic structure of the grown films has been investigated by ARPES. A weakly dispersive quasiparticle

<sup>\*</sup>Corresponding author: fengwei610@163.com<sup>†</sup>Corresponding author: zhuxiegang1984@163.com<sup>‡</sup>Corresponding author: lihuang.dmft@gmail.com

band was found at low temperature, indicating the  $f$  electrons are delocalized in the  $\alpha$  phase and hybridize with the conduction electrons. Temperature-dependent measurements reveal that the  $4f$ -derived peak near  $E_F$  exhibits a pronounced drop and both the ratio of the  $4f_{5/2}/4f_0$  and  $4f_{5/2}/4f_{7/2}$  states decreases obviously as increasing temperature. These results suggest that the  $f$  electrons become less localized in  $\alpha$ -Ce than in  $\gamma$ -Ce, which has been further certified from the comparison with theoretical calculations.

## II. EXPERIMENTAL AND COMPUTATIONAL DETAILS

Sample preparations and film growth were performed in several ultra high vacuum (UHV) chambers. These chambers are connected using a radical distribution chamber with a base pressure of  $5 \times 10^{-10}$  mbar. W(110) substrates were cleaned by cycles of  $\text{Ar}^+$  (2000 eV) at room temperature and flash annealing to 1300 K. Ce was evaporated from a tantalum crucible. After a long time outgassing of the Ce metal source, Ce was deposited onto the clean and well-ordered W(110) surface at room temperature. After the deposit of the fresh Ce films, the samples were transferred immediately to STM and ARPES chambers under UHV conditions. The base pressure was better than  $5 \times 10^{-10}$  mbar during evaporation. Thickness of the deposited Ce was monitored with a calibrated quartz oscillator.

STM experiments were performed in an ultrahigh vacuum, low temperature STM apparatus with a base pressure of  $5 \times 10^{-11}$  mbar. All the measurements were performed at 78 K with an electrochemically etched tungsten tip. All topography images were recorded in the constant current mode. ARPES measurements were performed with SPECS UVLS discharge lamp (21.2 eV, He- $\text{I}\alpha$  light). All data were collected with a Scienta R4000 electron analyzer. The overall energy resolution was 15 meV or better, and the typical angular resolution was  $0.2^\circ$ . A freshly evaporated gold sample was used to determine  $E_F$ . Temperature-dependent ARPES measurements were performed from high to low temperature.

For theoretical calculations, we tried to calculate the electronic structures of  $\alpha$  and  $\gamma$ -Ce with the combination of density functional theory and single-site dynamical mean-field theory (dubbed as DFT + DMFT) [28]. The DFT + DMFT method is probably the most powerful established approach to study the electronic structures of strongly correlated materials. It has been widely used to study the correlated  $4f$  or  $5f$  electron systems [29–31].

In the DFT part, the WIEN2K code was employed, which implements a full-potential linear augmented plane-wave formalism [32]. The experimental lattice structures of  $\alpha$  and  $\gamma$ -Ce were used [4]. The DFT calculations were done on a  $15 \times 15 \times 15$  Monkhorst-Pack  $k$  mesh (120  $k$  points in the irreducible Brillouin zone). The spin-orbit coupling effect was considered in the calculations. The muffin-tin radius for Ce was 2.50. We used  $R_{\text{MT}}K_{\text{MAX}} = 7.0$  and  $G_{\text{MAX}} = 9.0$  and chose the PBEsol functional [33] to express the exchange-correlation potential. For the DMFT part, we employed the EDMFTF software package [34] to do the calculations. Certainly, the  $4f$  orbitals in Ce were considered to be correlated. The Coulomb interaction matrix was parametrized by using the Slater integrals. The Coulomb interaction parameter  $U$  and

Hund's exchange parameter are 6.0 eV and 0.7 eV, respectively, which were in accordance with the previous DFT + DMFT calculations [35,36]. The double-counting term was treated with the fully-localized limit scheme [37]. We employed the hybridization expansion version continuous-time quantum impurity solver to solve the resulting seven-band Anderson impurity model [38,39]. The number of Monte Carlo sweeps per DMFT calculation is  $2.0 \times 10^9$ . The system temperatures were chosen to be  $T = 100$  K and 500 K for  $\alpha$  and  $\gamma$ -Ce, respectively. In order to accelerate the calculations, the Lazy trace evaluation trick was applied [40]. The Hilbert space for the local impurity problem was truncated, and only those atomic eigenstates with  $N \in [0,3]$  were retained [39]. We performed charge fully self-consistent DFT + DMFT calculations. Of the order of 40 DFT + DMFT iterations (which include about 800 DFT iterations and 40 one-shot DMFT calculations) were required to reach good convergence for the chemical potential and charge density. Once the charge density was converged, we then applied the maximum entropy method [41] to extract the real-frequency self-energy functions. Then we used them to evaluate the Fermi surfaces, momentum-resolved spectral functions  $A(\mathbf{k},\omega)$ , and density of states  $A(\omega)$ . The spectral functions, hybridization functions, and self-energy functions for  $\alpha$ -Ce and  $\gamma$ -Ce can be found in the Supplemental Material [42], which includes Refs. [1,10,11,16,37,43–49].

## III. RESULTS AND DISCUSSIONS

Structurally ordered Cerium films were grown at room temperature onto a W(110) substrate. About 100 Å Ce was deposited by evaporation from a tantalum crucible. Figure 1(a) shows the constant current STM image of the W(110) surface. After cycles of sputtering and annealing, many steps and terraces can be observed from the STM image and sharp spots can be seen from the LEED pattern, indicating the highly orientation of the W(110) surface. As fresh Ce is deposited onto the substrate, both ordered and disordered regions appear and only faint LEED spots can be observed, see Fig. 1(b). From the small range image of the ordered region in Figs. 1(d) and 1(e), many triangle and hexagonal pits can be seen. Figure 1(f) shows the profile along the line in Fig. 1(d), marked with  $aa'$ , from which the depth of the pits can be found to be about 3–8 Å. After annealing at 600 K for 5 minutes, both triangle and hexagonal pits disappear, instead, large triangle and hexagonal terraces appear [see Fig. 1(c)]. LEED spots become sharp, and also the area of the terraces becomes larger, indicating that the quality of the Ce films has been greatly improved after a short time annealing, and ordered Ce films can be obtained by this method. Appearance of both  $\beta$ -Ce(0001) (dhcp) and  $\gamma$ -Ce(111) (fcc) was reported for Ce thin films grown on W(110) [50]. Since the outermost two layers of both fcc(111) and dhcp(0001) surface are identical [22] and photoemission spectra in the low energy region of 21.2 eV are dominated by emissions of the two topmost layers due to the short mean free path of the photoelectrons, it is difficulty to distinguish the two phases by ARPES. Here the high-temperature (300 K) ordered Ce films are all called  $\gamma$ -Ce(111), instead the low-temperature Ce films (18 K) are called  $\alpha$ -Ce(111), following previous ARPES results [22,23].

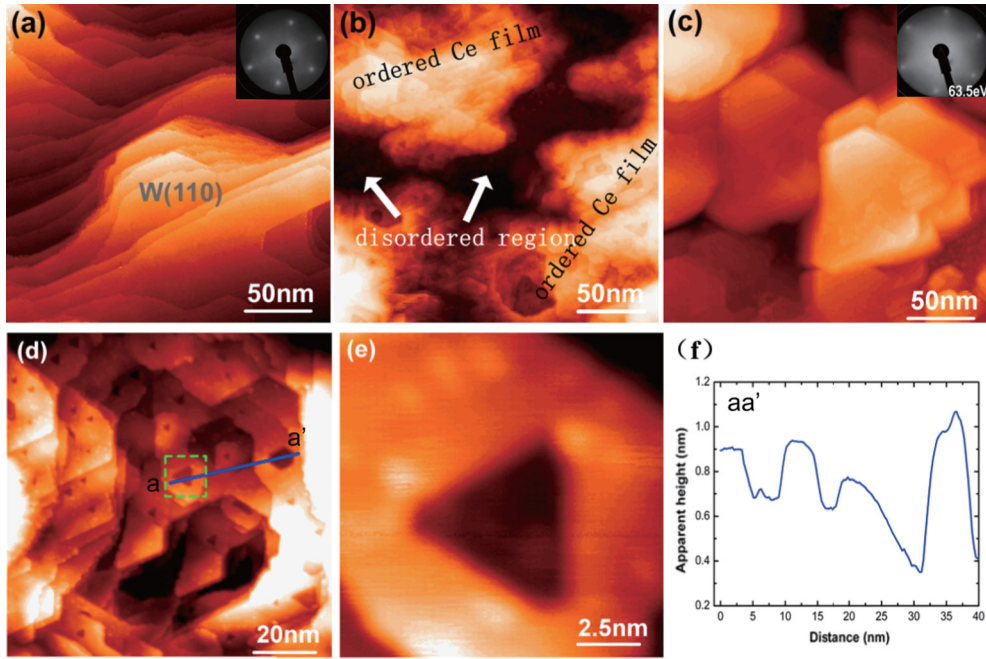


FIG. 1. (a) STM image of the W(110) substrate. (b) STM image of the freshly deposited Ce film. The inset is the LEED pattern of the W(110) substrate. (c)–(e) STM image of the ordered Ce film after annealing at 600 K with size of  $200 \times 200$  nm (c),  $100 \times 100$  nm (d), and  $10 \times 10$  nm (e). (f) Line profile of  $aa'$  in panel (d). The inset of panel (c) is LEED pattern of the ordered Ce film,  $E = 63.5$  eV. All the images are obtained with  $V_g = 1$  V, and  $I_t = 80$  pA.

The projected photoemission intensity map of the Ce(111) surface at 18 K with 21.2 eV photons is shown in Fig. 2(c). The Fermi surface consists of a rounded hole pocket centered at the  $\bar{\Gamma}$  point with “legs” extending to the  $\bar{M}$  and  $\bar{K}$  point. The topology of the Fermi surface can be more clearly identified from the constant-energy map at the binding energy of 150 meV in Fig. 2(d). Figure 2(e) shows the photoemission intensity plot along  $\bar{\Gamma}$ - $\bar{M}$ , and its corresponding curvature plot is displayed in Fig. 2(f). Five main features can be observed from the band structure, labeled A, B, C, D, and E in Fig. 2(f), respectively. Three of them are  $4f$ -derived features. Feature A at the binding energy (BE) of 1.91 eV is from the “poorly” screened Ce  $4f^0$  state, with valence electrons partially screening the hole, and is usually referred to as the ionization peak [51]. The one near  $E_F$  (B) is from the “well-screened” final state, with the  $4f$  hole filled by a valence electron and can be assigned to the  $4f_{5/2}^1$  state. The dispersionless band at 0.26 eV (C) is the spin-orbit component of the  $4f_{5/2}^1$  state, and is normally called the  $4f_{7/2}^1$  state [52]. A strongly dispersive band E from the conduction electrons can also be observed. Our results are somewhat different from previous ARPES studies measured at room temperature of ordered Ce films on W(110) [21–23]. In previous ARPES results, the  $4f$  photoelectron spectra of both  $\alpha$ - and  $\gamma$ -Ce reveal a characteristic double-peaked structure: one near  $E_F$  and the other at about 2.0 eV BE. The spin-orbit component of the  $4f_{5/2}^1$  state at 0.26 eV BE is hardly resolved in their results. The absence of the  $4f_{5/2}^1$  state in previous ARPES results on Ce films may be due to the limited energy resolutions (50–100 meV) and the matrix element. However, it is also observed in the photoemission study performed on polycrystalline Ce films on sapphire [53], from which the spin-orbit component at around 0.28 eV can also be observed.

The small energy difference is within experimental uncertainty. The appearance of the three  $4f$ -derived peaks is also evident from many other Ce-based heavy-fermion compounds, like  $\text{CeMIn}_5$  ( $M = \text{Co, Rh, Ir}$ ) [25] and  $\text{CeCoGe}_{1.2}\text{Si}_{1.2}$  [52].

Figure 3(a) zooms into the vicinity of  $E_F$  to concentrate on the hybridization of the conduction band and the  $f$  band at 18 K, and its corresponding energy distribution curves (EDCs) are displayed in Fig. 3(b). From Fig. 3(b), the spin-orbit component at 0.26 eV BE shows no dispersion, while for feature B, there exists a sharp crossover, within a single band form a dispersionless region around the  $\bar{\Gamma}$  point to dispersing peaks away from it. The reasonable way to explain this rather disjointed dispersion in a single band is that we observe the dominating  $f$  branch, which is very flat and lies slightly below  $E_F$  around the  $\bar{\Gamma}$  point. It hybridizes with the more dispersive band seen in higher BE. The hybridization of the  $f$  band and the conduction band can be well described by a simple mean-field hybridization band picture in Fig. 3(d), where  $\varepsilon_f$  is the renormalized  $f$ -level energy,  $\varepsilon_k$  is the conduction-band dispersion. When the conduction bands hybridize with the  $f$  band, the conduction bands start to bend when coming towards the energy level of the  $f$  band, and forms a weakly dispersive hybridized band near the  $f$  band energy level, which can be clearly observed from Fig. 3(b) and has been verified in the  $\text{CeCoIn}_5$  heavy-fermion compound [26].

We now turn our attention to the temperature dependence of the ARPES data. Figure 4(a) shows the ARPES data along  $\bar{\Gamma}$ - $\bar{M}$  for three temperatures at 18 K, 100 K, and 300 K, respectively, and their angle-integrated EDCs are displayed in Fig. 4(d). We here concentrate on the three  $4f$ -derived states in the ordered Ce films. All the intensities of the three peaks become weaker as temperature increases. From Fig. 4(d), the spectra taken at 18 K and 100 K are almost the same with each other, except

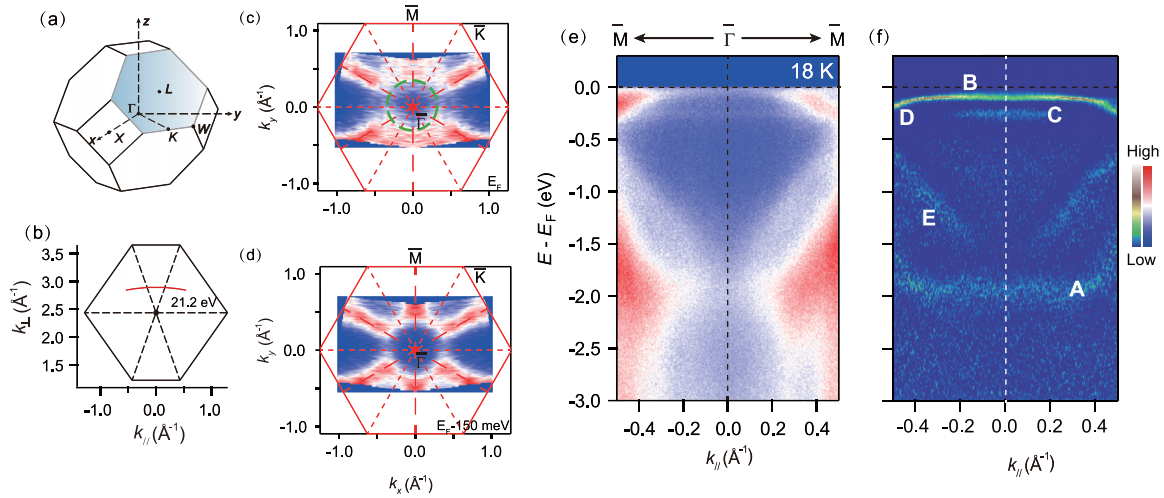


FIG. 2. (a) Brillouin zone of FCC lattice. (b) Sketch of the projected two-dimensional Brillouin zone,  $k$  trace of 21.2 eV photons has been marked with a red curve. An inner potential value of  $V_0 = 15$  eV is used here, which is a typical value for Cerium-based compounds [25,26]. Here  $k_{\perp}$  is perpendicular to the plane which has been marked blue in panel (a). (c) Projected photoemission intensity map of the Ce(111) surface at  $E_F$  integrated over a window of  $(E_F - 10 \text{ meV}, E_F + 10 \text{ meV})$ . The Brillouin zone is calculated with the lattice constant of  $a = b = 3.73 \text{ \AA}$  [22]. The  $f$  Fermi surface has been marked with the green circle. (d) Constant-energy map at the binding energy of 150 meV. (e) Photoemission intensity distribution along  $\bar{\Gamma}-\bar{M}$  taken at 18 K. (f) Curvature plot of panel (e). Five bands are labeled with different colors as A, B, C, D, and E. The formulas for the curvature and their applicability to experimental ARPES data have been demonstrated in Ref. [27].

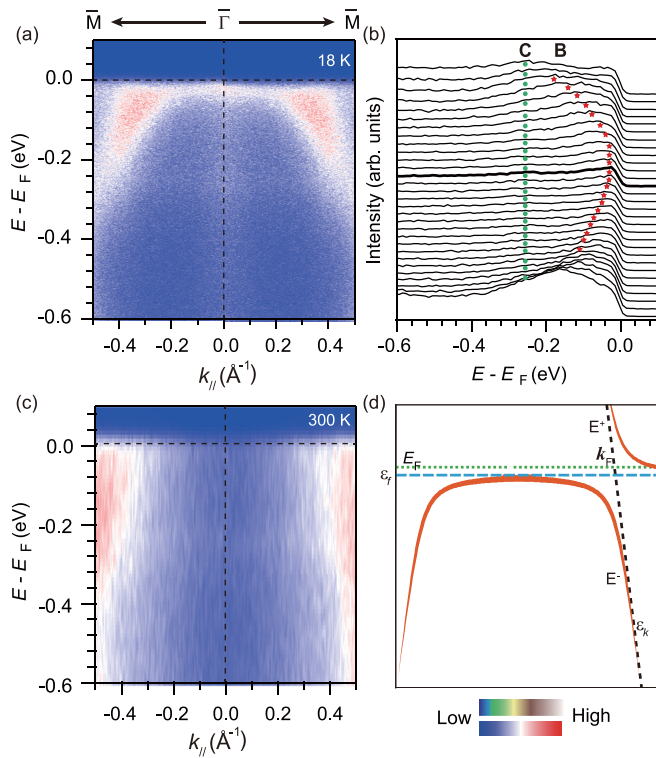


FIG. 3. (a) Photoemission intensity distribution of the ordered Ce films near  $E_F$  taken at 18 K. (b) The energy distribute curves of panel (a). Red and green markers serve as guides to the eye and represent the hybridized band and the spin-orbit component C, respectively. (c) Photoemission intensity distribution of the ordered Ce films near  $E_F$  taken at 300 K. (d) Schematic diagram of the hybridization between the  $f$  bands ( $\epsilon_f$ ) and a conduction band ( $\epsilon_k$ ) in panel (c) under a periodic Anderson model. The red curve is the hybridized band with thickness indicating the intensity of the spectral function.

a small amount of  $f$  intensity decrease at 100 K. However, obvious changes can be observed from the 18 K and 300 K data. At 300 K, a weak intensity of the  $4f_{5/2}^1$  peak near  $E_F$  in  $\gamma$ -Ce can be considered as indication for an almost localized  $4f^1$  ground state in this phase, see Figs. 3(c) and 4(d), while a strong

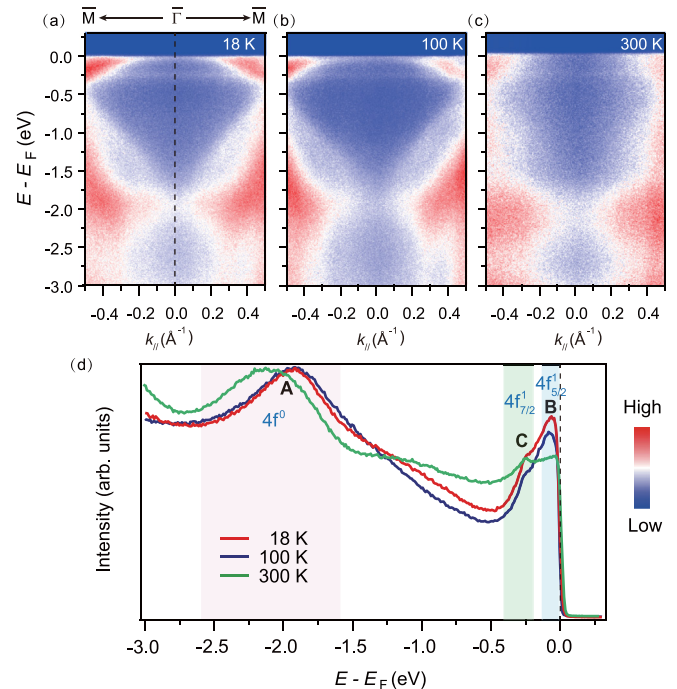


FIG. 4. (a)–(c) Photoemission intensity distributions of the ordered Ce films taken at 18 K (a), 100 K (b), and 300 K (c), respectively. (d) Angle-integrated EDCs of the ordered Ce films taken at different temperatures.

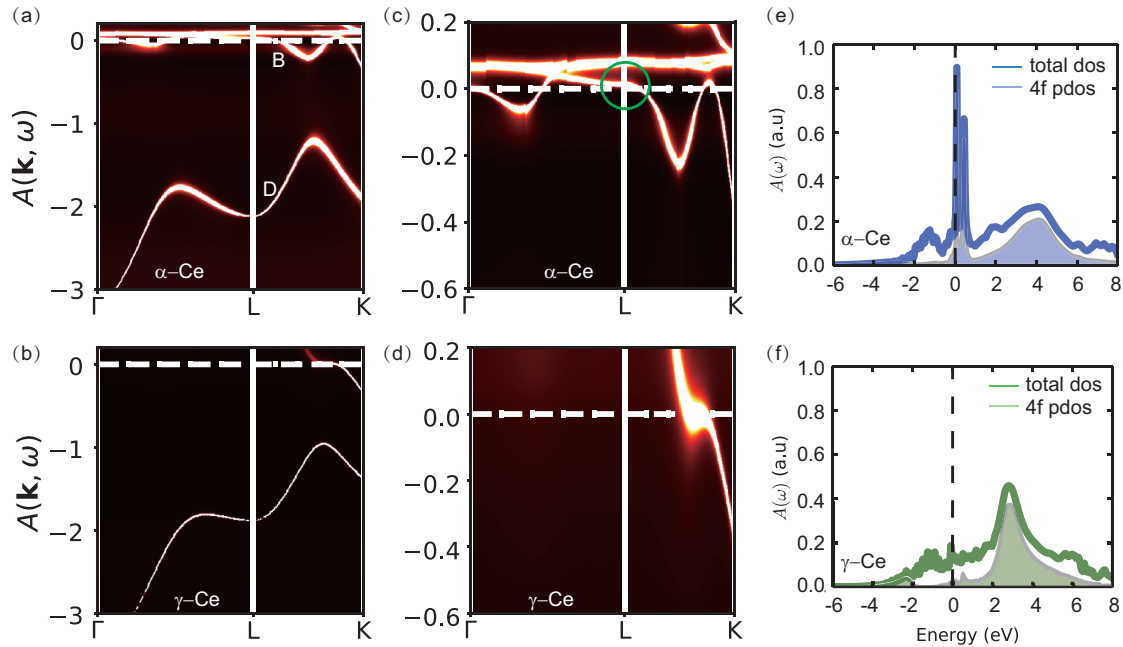


FIG. 5. (a),(b) Momentum-resolved spectral functions  $A(\mathbf{k}, \omega)$  of Ce by DFT+DMFT calculations. (a)  $\alpha$ -Ce, (b)  $\gamma$ -Ce. (c),(d) Momentum-resolved spectral functions  $A(\mathbf{k}, \omega)$  of Ce by DFT+DMFT calculations in a smaller energy range. (c)  $\alpha$ -Ce, (d)  $\gamma$ -Ce. The renormalized band near  $E_F$  has been marked out with a green circle. (e),(f) Total and  $4f$  partial density of states  $A(\omega)$ . (e)  $\alpha$ -Ce, (f)  $\gamma$ -Ce. The Fermi levels  $E_F$  are represented by vertical dashed lines. Note that the spectral data have been rescaled and normalized for a better visualization.

intensity of this peak in  $\alpha$ -Ce reflects increasing hybridization of  $4f$  and conduction electrons at low temperature. Moreover, the intensity ratios of the peak near  $E_F$  and that at around 0.26 eV is considerably larger in the  $\alpha$  phase than that in the  $\gamma$  phase. This is consistent with previous photoemission measurements performed on polycrystalline Ce, which was interpreted in the framework of Anderson impurity model [53]: In  $\gamma$ -Ce, the spin-orbit component at around 0.26 eV originates predominantly from the excitation of the  $4f_{7/2}^1$  level, when the hybridization parameter increases in  $\alpha$ -Ce, more  $4f_{7/2}$  character is admixed to the initial state, leading to a loss of atomic character which spreads and washed out the intensity of the  $4f_{7/2}$  structure.

We also observed obvious changes for the position of peak A. In the high-temperature  $\gamma$  phase, it lies at around 2.1 eV BE, which is consistent with previous ARPES data on  $\gamma$ -Ce(111) [22]. At low temperature, the position of this peak shifts to 1.9 eV BE, indicating an obvious change of the  $f$  character with temperature. The energy difference for the  $4f^0$  state in  $\gamma$  and  $\alpha$ -Ce was also observed on polycrystalline Ce [53].

The hybridization behavior can be further identified by comparing the spectral functions of  $\alpha$ - and  $\gamma$ -Ce using DFT+DMFT, as presented in Fig. 5. Since our ARPES data shown in Fig. 4 are taken along the  $\bar{\Gamma}$ - $\bar{M}$  direction of the projected Ce(111) surface, it can be compared with the spectral function along  $L$ - $K$  of bulk Ce by DFT+DMFT. From Figs. 5(a) and 5(b), differences can be observed only for the bands near  $E_F$  in the two phases. Figures 5(c) and 5(d) enlarge the spectral function of the two phases near  $E_F$ . For  $\alpha$ -Ce, obvious band renormalization can be observed near  $E_F$ , which results from hybridization between  $f$  bands and conduction bands, while it is absent in  $\gamma$ -Ce, indicating the  $f$  electron is

predominantly localized and did not participate in the Fermi surface construction. The contribution of  $f$  electrons near  $E_F$  in  $\alpha$ -Ce can also be evident from the  $f$  partial density of states in Figs. 5(e) and 5(f), from which it is clearly that large spectral intensity near  $E_F$  in  $\alpha$ -Ce is mainly from the  $f$  electrons. By comparing our experimental data with theoretical calculations, it is clear that only band D hybridizes with the  $f$  band near  $E_F$ , forming the weakly dispersive hybridized band and contributes a circle Fermi pocket around the zone center, which has been marked out with a green circle in Fig. 2(c). While for the conduction bands at higher banding energy (e.g., band E), it does not participate in the hybridization process and keeps the same in both  $\alpha$  and  $\gamma$  phase.

For heavy-fermion systems, due to  $c$ - $f$  hybridization between the conduction band and the Ce  $4f$  states, a dispersive quasiparticle band could be observed at the locations where  $f$  band and conduction band intersect, which has been confirmed in Fig. 3 and indicate that the  $f$  electrons hybridize with the conduction electrons at low temperature. Based on the framework of Anderson impurity model, with increasing coupling of the  $4f$  electrons to valence-band electrons, screening becomes more likely and the intensity of the screened  $4f^1$  emission feature increases at the expense of the unscreened  $4f^0$  feature, and vice versa. The stronger the  $f$  electrons hybridize with conduction electrons, the stronger the  $4f_{5/2}^1$  peak becomes, as shown in CeCoIn<sub>5</sub> and CeCoGe<sub>1.2</sub>Si<sub>0.8</sub> [26,52,54]. The ratio of the spectral intensity  $Ce4f^1/Ce4f^0$  can be used to verify the hybridization strength in the system. From Fig. 4(d), it is obvious that the ratio of  $Ce4f^1/Ce4f^0$  decreases significantly from 18 K to 300 K, which indicates the decreased hybridization in the  $\gamma$  phase. Moreover, previous resonant photoemission measurements performed on polycrystalline

Ce films suggested that the surface of  $\alpha$ -Ce metal shows  $\gamma$ -like behavior [55]. Since our ARPES measurements were performed with 21.2 eV photons, which is dominated by the contributions of the topmost 1–2 layers. It is reasonable to estimate that the ratio of the spectral intensity of  $Ce4f^1/Ce4f^0$  should be even larger in the bulk  $\alpha$ -Ce than that from our ARPES results.

Both the change of the  $4f^0$  peak position and the ratio of the spectral weight intensity  $Ce4f^1/Ce4f^0$  indicates that there is a change of the  $f$  electron character as a function of temperature during  $\gamma$ - $\alpha$  phase transition in metal Ce films. Based on the phase diagram of metal Ce, upon decreasing temperature, the  $\gamma$  phase transforms to the  $\beta$  phase at 326 K, and enters the  $\alpha$  phase at 96 K. The high-temperature  $\gamma$  phase displays a Curie-Weiss-like temperature dependence of the magnetic susceptibility, indicating the existence of the  $4f$ -derived local magnetic moments, while the  $\alpha$  phase has a Pauli-like temperature independent paramagnetism with rather delocalized  $f$  electrons [2]. At high temperature, a weak intensity of the Fermi-level peak in the  $\gamma$ -Ce can be considered as indication for an almost localized  $4f^1$  ground state in this phase, while a strong increase of this peak in  $\alpha$ -Ce at 18 K reflects increasing hybridization of  $4f$  and conduction bands. The  $f$ - $d$  hybridization gives rise to a sharp peak near  $E_F$ . Our ARPES data provide direct experimental evidence that the character of the  $f$  electrons changes from localized to delocalized in the  $\gamma$ - $\alpha$  transition.

#### IV. CONCLUSIONS

To summarize, we have grown well-ordered Ce metal films on a W(110) surface. The topography and electronic structure of the grown film has been studied by STM and ARPES, respectively. We find a weakly dispersive quasiparticle band at 18 K, indicating the hybridization between  $f$  electrons and conduction electrons at low temperature in the  $\alpha$  phase. Upon increasing temperature, the  $f$  electrons become localized at 300 K in the  $\gamma$  phase. The observed localized-to-itinerant transition with decreasing temperature during  $\gamma$ - $\alpha$  transition provides direct evidence that the characters of the  $f$  electrons play a very important role during the isostructural  $\gamma$ - $\alpha$  transition, which is further evident from the comparison with DFT+DMFT calculations. Our results on the epitaxial  $4f$  films may shed light on the interpretation of the driving force in the isostructural  $\gamma$ - $\alpha$  transition and investigation of the rich physical properties of the Kondo systems.

#### ACKNOWLEDGMENTS

This work is supported in part by the National Natural Science Foundation of China (Grant Nos. 11504342, 11504340, 11774320, and U1630248), Science Challenge Project (No. TZ2016004), National Key Research and Development Program of China (No. 2017YFA0303104), and the Dean Foundation of China Academy of Engineering Physics (Grant No. 201501040).

- 
- [1] J. W. Allen and R. M. Martin, *Phys. Rev. Lett.* **49**, 1106 (1982).
  - [2] R. V. Colvin, S. Aarj, and J. M. Peck, *Phys. Rev.* **122**, 14 (1961).
  - [3] C. R. Burr and S. Ehara, *Phys. Rev.* **149**, 551 (1966).
  - [4] J. Allen, S. Oh, O. Gunnarsson, K. Schönhammer, M. Maple, M. Torikachvili, and I. Lindau, *Adv. Phys.* **35**, 275 (1986).
  - [5] A. Fujimori and J. H. Weaver, *Phys. Rev. B* **32**, 3422 (1985).
  - [6] A. P. Murani, Z. A. Bowden, A. D. Taylor, R. Osborn, and W. G. Marshall, *Phys. Rev. B* **48**, 13981 (1993).
  - [7] T. Jarlborg, E. G. Moroni, and G. Grimvall, *Phys. Rev. B* **55**, 1288 (1997).
  - [8] M. Casadei, X. Ren, P. Rinke, A. Rubio, and M. Scheffler, *Phys. Rev. Lett.* **109**, 146402 (2012).
  - [9] M. Casadei, X. Ren, P. Rinke, A. Rubio, and M. Scheffler, *Phys. Rev. B* **93**, 075153 (2016).
  - [10] B. Johansson, I. A. Abrikosov, M. Aldén, A. V. Ruban, and H. L. Skriver, *Phys. Rev. Lett.* **74**, 2335 (1995).
  - [11] J. W. Allen and L. Z. Liu, *Phys. Rev. B* **46**, 5047 (1992).
  - [12] A. P. Murani, S. J. Levett, and J. W. Taylor, *Phys. Rev. Lett.* **95**, 256403 (2005).
  - [13] J. W. van der Eb, A. B. Kuz'menko, and D. van der Marel, *Phys. Rev. Lett.* **86**, 3407 (2001).
  - [14] D. Wieliczka, J. H. Weaver, D. W. Lynch, and C. G. Olson, *Phys. Rev. B* **26**, 7056 (1982).
  - [15] Y. Baer and G. Busch, *Phys. Rev. Lett.* **31**, 35 (1973).
  - [16] E. Wuilloud, H. R. Moser, W. D. Schneider, and Y. Baer, *Phys. Rev. B* **28**, 7354 (1983).
  - [17] M. Higashiguchi, K. Shimada, T. Narimura, H. Namatame, and M. Taniguchi, *Physica B: Condensed Matter* **351**, 256 (2004).
  - [18] L. Z. Liu, J. W. Allen, O. Gunnarsson, N. E. Christensen, and O. K. Andersen, *Phys. Rev. B* **45**, 8934 (1992).
  - [19] M. Grioni, P. Weibel, D. Malterre, Y. Baer, and L. Du'ò, *Phys. Rev. B* **55**, 2056 (1997).
  - [20] G. Rosina, E. Bertel, F. P. Netzer, and J. Redinger, *Phys. Rev. B* **33**, 2364 (1986).
  - [21] D. V. Vyalikh, Y. Kucherenko, S. Danzenbächer, Y. S. Dedkov, C. Laubschat, and S. L. Molodtsov, *Phys. Rev. Lett.* **96**, 026404 (2006).
  - [22] F. Schiller, M. Heber, V. D. P. Servedio, and C. Laubschat, *Phys. Rev. B* **68**, 233103 (2003).
  - [23] O. Morimoto, H. Kato, Y. Enta, and Y. Sakisaka, *Surf. Sci.* **603**, 2145 (2009).
  - [24] C. Gu, X. Wu, C. G. Olson, and D. W. Lynch, *Phys. Rev. Lett.* **67**, 1622 (1991).
  - [25] S.-I. Fujimori, A. Fujimori, K. Shimada, T. Narimura, K. Kobayashi, H. Namatame, M. Taniguchi, H. Harima, H. Shishido, S. Ikeda, D. Aoki, Y. Tokiwa, Y. Haga, and Y. Onuki, *Phys. Rev. B* **73**, 224517 (2006).
  - [26] Q. Y. Chen, D. F. Xu, X. H. Niu, J. Jiang, R. Peng, H. C. Xu, C. H. P. Wen, Z. F. Ding, K. Huang, L. Shu, Y. J. Zhang, H. Lee, V. N. Strocov, M. Shi, F. Bisti, T. Schmitt, Y. B. Huang, P. Dudin, X. C. Lai, S. Kirchner, H. Q. Yuan, and D. L. Feng, *Phys. Rev. B* **96**, 045107 (2017).
  - [27] P. Zhang, P. Richard, T. Qian, Y.-M. Xu, X. Dai, and H. Ding, *Rev. Sci. Instrum.* **82**, 043712 (2011).
  - [28] G. Kotliar, S. Y. Savrasov, K. Haule, V. S. Oudovenko, O. Parcollet, and C. A. Marianetti, *Rev. Mod. Phys.* **78**, 865 (2006).

- [29] H. Lu and L. Huang, *Phys. Rev. B* **94**, 075132 (2016).
- [30] J. H. Shim, K. Haule, and G. Kotliar, *Science* **318**, 1615 (2007).
- [31] J. H. Shim, K. Haule, and G. Kotliar, *Nature (London)* **446**, 513 (2007).
- [32] P. Blaha, K. Schwarz, G. Madsen, D. Kvasnicka, and J. Luitz, *WIEN2K, An Augmented Plane Wave + Local Orbitals Program for Calculating Crystal Properties* (Karlheinz Schwarz, Techn. Universitt Wien, Austria, 2001).
- [33] J. P. Perdew, A. Ruzsinszky, G. I. Csonka, O. A. Vydrov, G. E. Scuseria, L. A. Constantin, X. Zhou, and K. Burke, *Phys. Rev. Lett.* **100**, 136406 (2008).
- [34] K. Haule, C.-H. Yee, and K. Kim, *Phys. Rev. B* **81**, 195107 (2010).
- [35] K. Haule, V. Oudovenko, S. Y. Savrasov, and G. Kotliar, *Phys. Rev. Lett.* **94**, 036401 (2005).
- [36] B. Chakrabarti, M. E. Pezzoli, G. Sordi, K. Haule, and G. Kotliar, *Phys. Rev. B* **89**, 125113 (2014).
- [37] V. I. Anisimov, F. Aryasetiawan, and A. I. Lichtenstein, *J. Phys.: Condens. Matter* **9**, 767 (1997).
- [38] E. Gull, A. J. Millis, A. I. Lichtenstein, A. N. Rubtsov, M. Troyer, and P. Werner, *Rev. Mod. Phys.* **83**, 349 (2011).
- [39] K. Haule, *Phys. Rev. B* **75**, 155113 (2007).
- [40] P. Sémon, C.-H. Yee, K. Haule, and A.-M. S. Tremblay, *Phys. Rev. B* **90**, 075149 (2014).
- [41] M. Jarrell and J. Gubernatis, *Phys. Rep.* **269**, 133 (1996).
- [42] See Supplemental material at <http://link.aps.org/supplemental/10.1103/PhysRevB.97.155155> for localized to itinerant transition of  $f$  electrons in the ordered Ce films on W(110).
- [43] D. M. Wieliczka, C. G. Olson, and D. W. Lynch, *Phys. Rev. B* **29**, 3028 (1984).
- [44] M. B. Zöfl, I. A. Nekrasov, T. Pruschke, V. I. Anisimov, and J. Keller, *Phys. Rev. Lett.* **87**, 276403 (2001).
- [45] K. Held, A. K. McMahan, and R. T. Scalettar, *Phys. Rev. Lett.* **87**, 276404 (2001).
- [46] A. K. McMahan, *Phys. Rev. B* **72**, 115125 (2005).
- [47] A. K. McMahan, K. Held, and R. T. Scalettar, *Phys. Rev. B* **67**, 075108 (2003).
- [48] B. Amadon, T. Applencourt, and F. Bruneval, *Phys. Rev. B* **89**, 125110 (2014).
- [49] B. Johansson, *Philos. Mag.* **30**, 469 (1974).
- [50] Y. Aoki, H. Sato, Y. Komaba, Y. Kobayashi, H. Sugawara, S. Hashimoto, T. Yokoyama, and T. Hanyu, *Phys. Rev. B* **54**, 12172 (1996).
- [51] M. R. Norman, D. D. Koelling, A. J. Freeman, H. J. F. Jansen, B. I. Min, T. Oguchi, and L. Ye, *Phys. Rev. Lett.* **53**, 1673 (1984).
- [52] H. J. Im, T. Ito, H.-D. Kim, S. Kimura, K. E. Lee, J. B. Hong, Y. S. Kwon, A. Yasui, and H. Yamagami, *Phys. Rev. Lett.* **100**, 176402 (2008).
- [53] F. Patthey, B. Delley, W. D. Schneider, and Y. Baer, *Phys. Rev. Lett.* **55**, 1518 (1985).
- [54] S. I. Fujimori, T. Okane, J. Okamoto, K. Mamiya, Y. Muramatsu, A. Fujimori, H. Harima, D. Aoki, S. Ikeda, H. Shishido, Y. Tokiwa, Y. Haga, and Y. Ōnuki, *Phys. Rev. B* **67**, 144507 (2003).
- [55] E. Weschke, C. Laubschat, T. Simmons, M. Domke, O. Strebler, and G. Kaindl, *Phys. Rev. B* **44**, 8304 (1991).